NANO · MICRO small
www.small-journal.com

Quantitative Element-Sensitive Analysis of Individual Nanoobjects

André Wählisch, Rainer Unterumsberger, Philipp Hönicke,* Janin Lubeck, Yves Kayser, Jan Weser, Gaoliang Dai, Kai Hahm, Thomas Weimann, Christian Seim, Stefan Rehbein, and Burkhard Beckhoff*

A reliable and quantitative material analysis is crucial for assessing new technological processes, especially to facilitate a quantitative understanding of advanced material properties at the nanoscale. To this end, X-ray fluorescence microscopy techniques can offer an element-sensitive and non-destructive tool for the investigation of a wide range of nanotechnological materials. Since X-ray radiation provides information depths of up to the microscale, even stratified or buried arrangements are easily accessible without invasive sample preparation. However, in terms of the quantification capabilities, these approaches are usually restricted to a qualitative or semi-quantitative analysis at the nanoscale. Relying on comparable reference nanomaterials is often not straightforward or impossible because the development of innovative nanomaterials has proven to be more fast-paced than any development process for appropriate reference materials. The present work corroborates that a traceable quantification of individual nanoobjects can be realized by means of an X-ray fluorescence microscope when utilizing rather conventional but well-calibrated instrumentation instead of reference materials. As a proof of concept, the total number of atoms forming a germanium nanoobject is quantified using soft X-ray radiation. Furthermore, complementary dimensional parameters of such objects are reconstructed.

1. Introduction

New and promising nanostructured materials are constantly being developed at an increasing pace and for a broad range of applications.[1–3] One prominent field that heavily relies on applying nanomaterials is the semiconductor industry. There, state-of-the-art integrated devices incorporate a multitude of materials in a highly complex manner.[4–9] In fact, according to Orji et al.,[10] the semiconductor industry is reaching a point at which the position and type of every atom within a device must be known. Many metrological methods, such as scanning probe microscopy, electron-based techniques, and X-ray-based probes,[11] are being applied and developed for the characterization of these nanostructures. They allow for the investigation of different physical or chemical properties, enabling a systematic evaluation and tuning of the desired functional properties.[10,12,13] However, existing metrology options are approaching inherent limits and require significant advances to keep up with future technology needs.[14] For example, sub-surface or buried nanoobjects stacked on top of each other are either inaccessible to techniques such as scanning electron microscopy or can be made accessible only very localized (e.g., using cross-sectional transmission electron microscopy). In that case, this approach entails high preparative effort and destroys the device. Consequently, there is a considerable need for characterization techniques that can address these limitations, that is, provide non-destructive, rapid, and multidimensional feedback.[15]

Methods based on X-ray fluorescence (XRF) can provide such non-invasive insights into the elemental composition of a wide range of materials.[16–18] Due to information depths of up to several µm, even sub-surface parts of nanostructures are easily accessible. Recent works[19,20] highlight the capability to simultaneously provide dimensional and analytical information for an ensemble of structures. Nevertheless, the analytical reliability of most XRF applications is often strongly dependent on the availability of appropriate reference materials.[21–23] These reference materials must have similar morphology and elemental composition as the specimen of interest, which ensures comparability. The production of these materials is, therefore,

A. Wählisch, R. Unterumsberger, P. Hönicke, J. Lubeck, Y. Kayser, J. Weser, B. Beckhoff
Physikalisch-Technische Bundesanstalt (PTB)
Abbestr. 2-12 10587, Berlin, Germany
E-mail: andre.waehlisch@ptb.de; philipp.hoenicke@ptb.de
G. Dai, K. Hahm, T. Weimann
Physikalisch-Technische Bundesanstalt (PTB)
Bundesallee 100 38116, Braunschweig, Germany
C. Seim
Technische Universität Berlin
Germany, Hardenbergstr. 36 10623, Berlin, Germany
S. Rehbein
Helmholtz-Zentrum Berlin für Materialien und Energie
Albert-Einstein-Str. 15 12489, Berlin, Germany
The ORCID identification number(s) for the author(s) of this article can be found under https://doi.org/10.1002/smll.202204943.

DOI: 10.1002/smll.202204943

usually associated with high manufacturing and characterization efforts. Consequently, the number of studied nanostructured materials is growing much faster than the availability of well-performing reference materials.[24–26]

An alternative and inherently different approach is given by reference-free XRF,[27] which does not rely on any reference materials. Instead, this approach is based on calibrated instrumentation and good knowledge of the atomic fundamental parameters that are related to the physical interaction processes. The general lack of nanoscale reference materials can therefore be addressed by reference-free XRF, which is also capable of qualifying calibration samples.[28,29] The resulting flexibility of this methodology enables the rapid application to a broad range of material systems, even when conventional approaches fail to provide the desired quantitative information. This work demonstrates that the applicability of reference-free XRF can be extended down to individual nanoscopic objects. It is shown that a reliable quantification of the number of atoms forming the nanoobject can be achieved by means of a high spatial resolution photon probe approach in combination with calibrated instrumentation. The general principles presented in this work are easily transferable to similar X-ray fluorescence microscope (XFM) set-ups and their application fields.[23,30,31] Furthermore, it is shown here that dimensional parameters, such as length, width, and height, can be derived with a novel model-based reconstruction. This reconstruction is possible even when the probing X-ray beam is slightly larger than the objects themselves. Based on supporting simulations, the generality of the approach is illustrated and how it may be applied for the investigation of state-of-the-art and future semiconductor devices.

2. Results and Discussion

The general principle of the utilized XFM set-up is illustrated in **Figure 1**. A soft X-ray beam, provided by an undulator beamline, is focused by means of a Fresnel zone plate and used to illuminate the sample locally. The photon-induced X-ray fluorescence radiation is emitted from an area on the sample about the same size as the excitation beam. Thus, the analysis of the emitted X-ray fluorescence enables a quantitative and element-sensitive characterization on the length scale of the excitation spot size on the order of 100 nm, that is, nano-XRF. Moreover, all expertise on well-established conventional XRF applications (without focusing optic) can be readily transferred to the XFM because it is based on the same general principles. In particular, this transferability includes the utilization of calibrated instrumentation,[27] preserving crucial traceability characteristics without relying on any (nano) reference materials. To validate this transfer, two independent quantitative experiments on the same laterally homogeneous sample are compared in **Table 1**, one with conventional reference-free XRF and one with the nanofocused XFM set-up.

The comparison shows good agreement of the results within the respective uncertainties. When investigating nanoscaled objects, such as particles or regularly ordered nanostructures, grazing emission X-ray fluorescence[33] is advantageous in regard to increased measurement throughput and discrimination capabilities. Nevertheless, it is limited to probing an entire ensemble of objects and provides averaged results on all objects within the field of view of the probing beam. However, the complementary element-sensitive study of individual nanoobjects is also often desirable. Accordingly, for the methodological development and subsequent demonstration of XRF quantification at a nanoscale lateral resolution of individual nanoobjects, several germanium structures were fabricated by electron beam lithography (EBL).

1. An individual rectangular cuboid, which is not surrounded by any other structures (length, width, and height of the object are approximately 1000 nm, 150 nm, and 30 nm, respectively, cf. **Figure 2**a). Two rectangular cuboids close to each other forming a tapered region with a minimal distance of about 40 nm (Figure 2b).
3. Larger objects with widths of up to 50 µm from the same EBL run (not shown here), which were used for beam profile determinations and complementary X-ray reflectometry (XRR).

The cuboid nanostructures were laterally raster-scanned using the XFM set-up. Horizontal and vertical sampling step sizes were 100 nm, which is smaller than the lateral dimensions

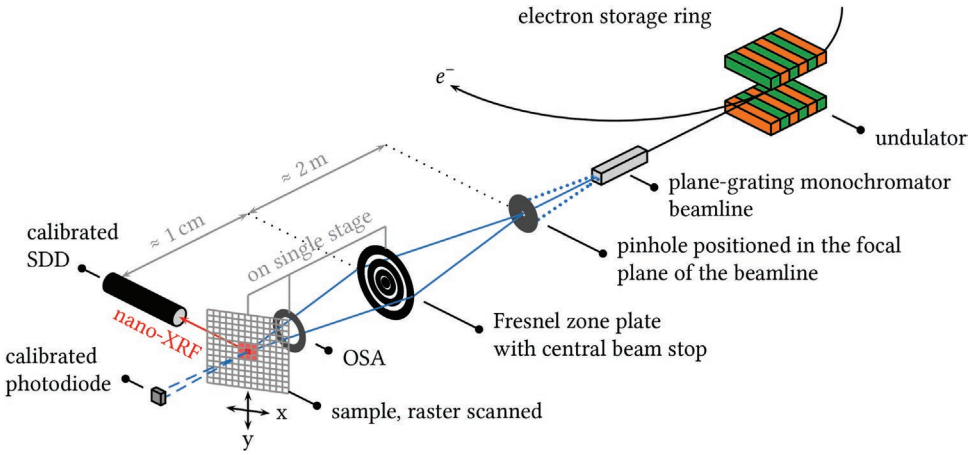

Figure 1. Schematic illustration of the XFM set-up at PTB's plane grating monochromator beamline at BESSY II. Distances and sizes are not drawn to scale.

Table 1. Independent quantification results of a single homogeneous germanium layer with a nominal thickness of 15 nm.

Methodology	Ge mass thickness/μg cm^{-2}
Reference-free XRF	6.7 (4)
Reference-free nano-XRF	7.0 (4)

of the investigated objects themselves and smaller than the pre-characterized beam size of about 160 nm, that is, with sufficient overlap. The resulting quantitative X-ray fluorescence maps are shown in Figure 2.

From these quantitative maps, the total germanium mass and equally the number of germanium atoms of the individual cuboid and the tapered set of cuboids can be determined, as given in Figure 2. This is achieved by deriving a position-dependent mass thickness (g cm^{-2}) as in conventional (non-focused) reference-free XRF analysis[27] for each measurement position and numerically integrating over both lateral directions[34] for the entire ensemble of positions. It should be emphasized that this process of integration relies on oversampling the entire specimen but is model-free and does not require any a priori knowledge about the sample geometry. Thus, it is easily applicable to more complex nanosystems. These include highly heterogeneous systems, for example, in the areas of biological,[16] nanotechnological,[13] and energy material[17] applications, for which the availability of reference materials is very limited.

Instead of integrating the X-ray fluorescence maps and thereby discarding the contained dimensional information of the nanoobject, it is also possible to preserve the spatial information of each measurement position. This is achieved with a novel model-based reconstruction algorithm, using ray tracing simulations to derive the influence of the involved complex geometric effects. The simulation takes into account the pre-characterized beam profile, a geometric model of the specimen itself, and the spatial arrangement with regard to the X-ray fluorescence detector. The position-dependent X-ray fluorescence intensity is then calculated for a specific set of dimensions and the position of the sample. Consequently, it is possible to reconstruct these properties of the specimen when compared to the experimental data. The individual cuboid objects' length, width, and height were accordingly determined as model parameters by means of numerical optimization. Thus, the presented XFM approach can simultaneously provide both element-sensitive analytical and dimensional characterization. For further details about the reconstruction approach, see the Section 4.

The reconstruction requires a priori knowledge about the sample geometry characteristics in order to parametrize a spatial model. For example, the structures are manufactured with clearly rectangular shapes by the EBL technique as verified by the SEM and AFM measurements (cf. Figure 2 and Figure 5) and, therefore, can be modelled as regular cuboids. Hence, for dedicated structures created by a well-controlled process, an introduced model error will be either negligible or, conversely, could be used to discriminate between different geometrical shapes. To extract the optimal model parameters and determine their uncertainties, a Markov-Chain-Monte-Carlo (MCMC) algorithm[35] was applied. This algorithm performs a simulation of the detected germanium X-ray fluorescence photon flux as a function of the beam position relative to the structures. In an iterative manner, the algorithm compares these calculated values to the experimental data. Minimizing the deviations between calculation and measurement, through adjustment of the model parameters, allows a probability density function for each model parameter to be estimated. One example of a resulting histogram is given in **Figure** 3, showing the distribution of the relative probability of different cuboid heights for the separate object. A mean value and its uncertainty, that is, a standard deviation, are readily extracted.

The reconstruction quality can be seen from the projectional insets of Figure 2 below and next to the respective X-ray fluorescence maps. Except for some overestimated smoothness due to the assumed perfectly rectangular shape, the reconstruction reproduces the experimental data. The quantitative results of the reconstruction, that is, object length *l*, width *w*,

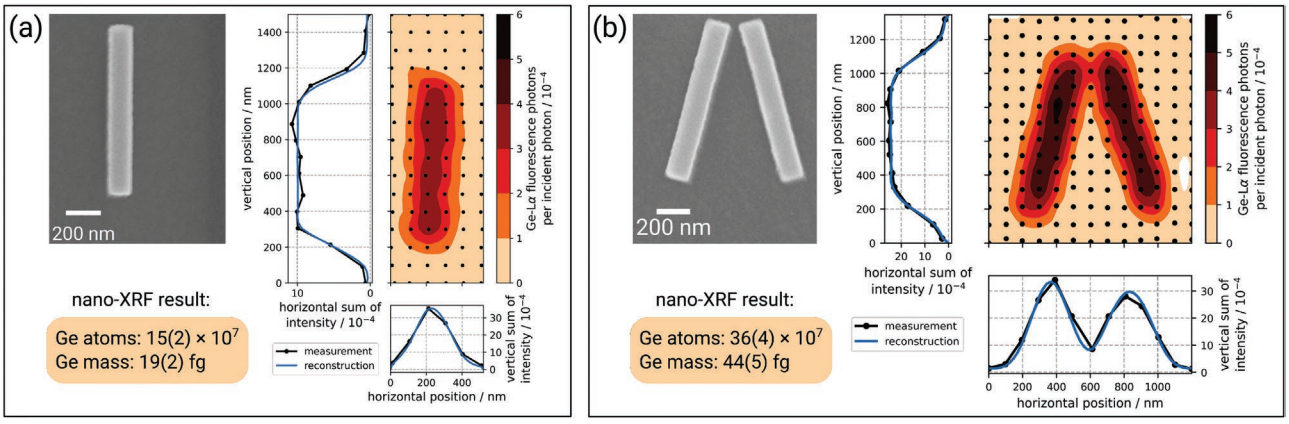

Figure 2. SEM images and experimentally determined Ge-Lα X-ray fluorescence maps of separate nanoobject (a) and tapered set of cuboids (b). Depicted SEM images are from sister samples from the same EBL run as those measured with the XFM set-up. Each black dot in the X-ray fluorescence maps marks a measured position. Horizontally and vertically summed intensities are shown for a descriptive comparison between measurement (black) and reconstruction (blue). In addition to the quantification result of the elemental mass, the corresponding number of germanium atoms is derived based on the atomic mass of germanium.

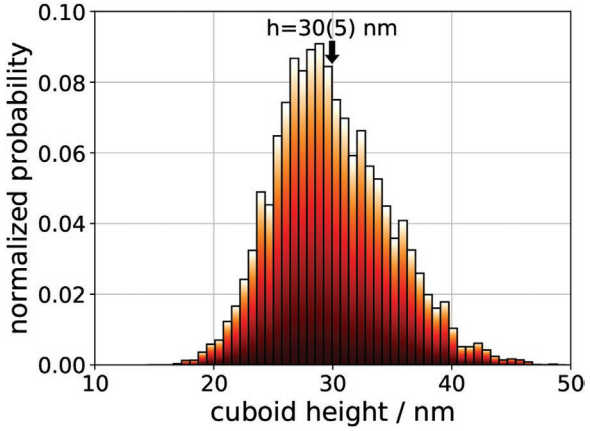

Figure 3. Histogram of the cuboid height as derived from the MCMC simulation, taking into account all involved instrumental, experimental and atomic fundamental parameters, including their respective uncertainties. The mean value of the height *h* and its respective uncertainty, in the form of the standard deviation, are readily extracted from this histogram.

and height *h*, are listed in **Table 2**. The uncertainty of the lateral width and length values derived by MCMC acutely depends on the specific interplay of step size, beam width, object size and the (to some extent arbitrary) object positioning—especially in regard to sensitive edge positions of the respective lateral direction—as it can be observed for the separate cuboid. SEM measurements showed nearly identical widths and lengths of the two tapered objects. Hence, for the nano-XRF reconstruction, only a single width and length were assumed, respectively. These spatial parameters can be used to derive the total germanium mass $m = \rho lwh$ based on the volume and the density (ρ), resulting in nearly identical values compared to the spatial integration approach. In addition, the results of atomic force microscopy (AFM) and scanning electron microscopy (SEM) measurements performed on identical sister samples are listed in Table 2. Generally, when comparing the results of these distinct methods, a good quantitative agreement is evident within the stated uncertainties. The determined length and width from SEM differ by a few per cent in comparison to the other two approaches. A likely reason for this is that the employed SEM device is off-the-shelf with only estimated quality of calibration. Since all three methods rely on different physical working principles and were performed independently of each other, the apparent consistency provides a mutual validation. The utilized AFM[36,37] is a carefully calibrated state-of-the-art tool for dimensional metrology. Hence, the achieved uncertainties are lower than those of the nano-XRF. For the compositionally simple benchmark systems, the elemental discrimination capability of XRF could not be demonstrated. But for more complex sample structures with multiple elemental constituents, the possibility to distinguish the characteristic X-ray fluorescence radiation emitted by different elements becomes a major advantage.

The semiconductor industry is a prominent area of applications where devices consist of highly complex nanostructures. Here, continuous scaling efforts towards increasingly efficient devices[38] are accompanied by an increase in complexity, that is, complexity in design and fabrication and, accordingly, complexity in composition and structure.[7,39–41] State-of-the-art X-ray microscopes optimized for spatial resolution have already achieved sub-10 nm resolution, even in the soft X-ray regime.[42] Thus, the demonstrated nano-XRF approach could be a promising candidate for analyzing semiconductor nanostructures with similar sizes. To showcase the expectable discrimination capabilities of nano-XRF, simulations of a theoretical nano-XRF experiment were performed for one possible future transistor system, namely, the forksheet architecture.[41] Several etching processes are required to form these sophisticated 3D structures. One of these processes is the removal of sacrificial silicon-germanium (SiGe) material without altering the rest of the device. If too much sacrificial material remains, the formation of properly working devices can be hindered, cf. **Figure** 4a. A simulation, shown in Figure 4b, illustrates how a nano-XRF line scan during a particular etching stage can discriminate the total amount of material remaining (given by the area under each curve) and also the location of this material: The blue curve describes a uniform partial etching of SiGe, the orange curve describes a non-uniform and therefore erroneous etching given by additional material remaining at a specific location. The general lateral location of this erroneous etching can already be estimated directly from the line scan. Applying a reconstruction based on a model of this system can be used to deduce the exact arrangement, including the vertical position. Similar arguments can readily be used for investigations of the homogeneity *along* the forksheet structures. This kind of information could be valuable input during the development of such complex device design processes.

It is beneficial to compare the traceable quantification capabilities of nano-XRF to scanning electron microscopy/energy

Table 2. Dimensional parameters of the separate cuboid and tapered nanostructures derived from the reference-free nano-XRF reconstruction compared to SEM, AFM and XRR data. AFM and SEM measurements were conducted on sister samples produced in the same run with identical nominal parameters. XRR was performed on a proxy sample with nominally equal height but a width of 50 µm and a length of several mm from the same run. The given AFM uncertainty values are the expanded measurement uncertainty evaluated with a coverage factor of $k = 2$. All other uncertainty values are derived with a coverage factor of $k = 1$.

	Separate cuboid			Tapered structure		
Method	Width/nm	Length/nm	Height/nm	Width/nm	Length/nm	Height/nm
Nano-XRF	140(20)	931(5)	32(6)	131(17)	964(62)	31(4)
AFM	143(2)	–	35(1)	–	–	–
SEM	144(5)	990(5)	–	151(5), 149(5)	989(5), 993(5)	–
XRR	–	–	32.8(5)	–	–	32.8(5)

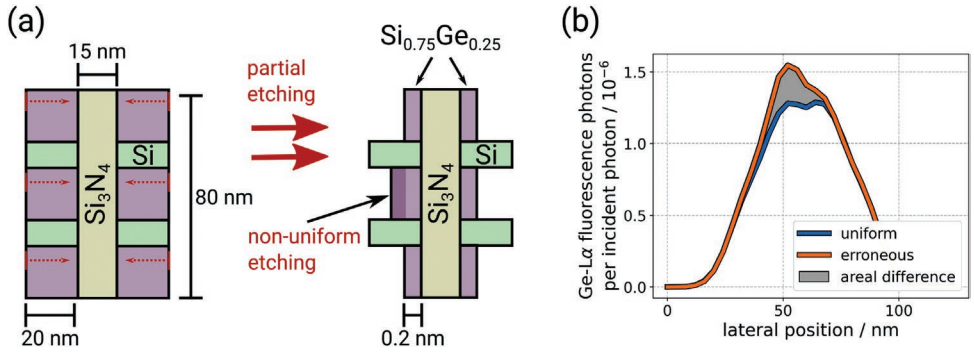

Figure 4. a) Schematic illustration of a SiGe etching process during the formation of a forksheet structure (cross-sectional view). The left part of the image depicts the sacrificial SiGe material before etching with a total lateral width of 20 nm. The right part depicts a partial and erroneous etching, where more material remains at a specific position compared to other locations of SiGe. b) Simulated line scan of germanium Lα X-ray fluorescence intensity emitted by the forksheet structure, after partial SiGe removal (15 nm beam FWHM, 4 nm sampling step size). The blue curve represents a uniform partial etching of SiGe at all locations, after a reduction from 20 nm down to 0.2 nm lateral width, that is, a removal of almost all but 1% of sacrificial material. The orange curve describes an erroneous partial etching, that is, a specific location (as indicated in the left figure) is only etched down to 0.3 nm instead of 0.2 nm. The shaded area indicates the areal difference of the curves and amounts to roughly 8%, which can directly be converted to an absolute amount of SiGe material.

dispersive X-ray spectrometry (SEM/EDS), a technique relying on electrons instead of photons to induce X-ray fluorescence radiation. SEM/EDS has many similarities to scanning nano-XRF analysis because of basically identical detection channels. While SEM/EDS set-ups usually have access to superior spatial resolution in the excitation channel (about 1 nm), they face other challenges.[43,44] These include, for example: Considerably higher bremsstrahlung background limiting the sensitivity achievable, limited penetration depth barring the access to buried structures, intricate geometric effects hindering a straightforward analysis, large uncertainties in atomic fundamental parameters related to the electron-material interaction process and charging effects necessitating a conductive coating. All of these are subject to errors with respect to the quantification scheme, limiting the usefulness of SEM/EDS in this regard. Nevertheless, both methods would undoubtedly benefit from mutual validation for the purpose of examining methodological shortcomings and leveraging complementary advantages.

3. Conclusion

In summary, this work successfully transfers reference-free XRF quantification capabilities to an X-ray fluorescence microscope. This quantification enables the determination of the elemental mass of an individual nanoobject or, equivalently, the number of atoms forming it. The presented approach can be applied to a wide range of materials because the underlying spatial integration is model-free and does not depend on the availability of any reference materials. Moreover, it has been shown that a reconstruction can provide dimensional insights if a geometrical model of the sample can be defined, for example, if the manufacturing process is well understood. Since this reconstruction approach is flexible with respect to both the materials employed and the complexity of the nanoobjects, it can also be applied to real-world nanoobjects, that is, to more complex systems than the presented benchmark structures. This complexity may raise the required computational cost. For example, when taking the X-ray attenuation of materials stacked on top of each other into account.

The general principles of the approach, which relies on the use of calibrated instrumentation and good knowledge of atomic fundamental parameters, are readily transferable to similar XFM set-ups. Even though such calibration of X-ray detectors requires a certain effort, this is more than compensated by the potential to probe nearly any material quantitatively. The actual spatial resolution of the used set-up is relatively moderate compared to state-of-the-art set-ups designed for the highest spatial resolution. However, the presented quantification and reconstruction methodologies are easily scalable. If the resolution of the excitation channel is improved, this will allow for the characterization of equally smaller objects. The important aspect of beam damage, which is otherwise often negligible, becomes relevant when applying the approach with increasingly high excitation intensity and to especially sensitive structures (e.g., biological matter). This could mean that the specimen gets damaged before it is sufficiently probed. Maximizing the detection efficiency by using detectors with increased detector area can be crucial[45] but calls for more complex instrumental calibration strategies.

4. Experimental Section

Materials: Samples were fabricated on a silicon (100) wafer using EBL. The fabrication procedure consists of depositing a 130 nm PMMA resist (ARP 671.02) on top of the cleaned substrate, which was then exposed by EBL. It was performed using a Vistec EBPG 5000+ e-beam system (at 50 kV and a corresponding dose of 470 µC cm^{-2}). The resist was developed in a solution of isopropyl alcohol and methyl isobutyl ketone (3:1) + 1% methyl ethyl ketone for 45 s. The realization of the nanostructured germanium was then obtained by deposition of a nominally 30 nm thick germanium film, followed by the lift-off process. The germanium was deposited by the thermal evaporation technique at a pressure of 10^{-6} mbar and temperatures of up to 160 °C.

AFM Measurements: A representative AFM line scan is shown in **Figure 5**. The measurement is performed with a CD-AFM developed at the PTB.[36] The CD-AFM applies a six-axis flexure hinge nanopositioning

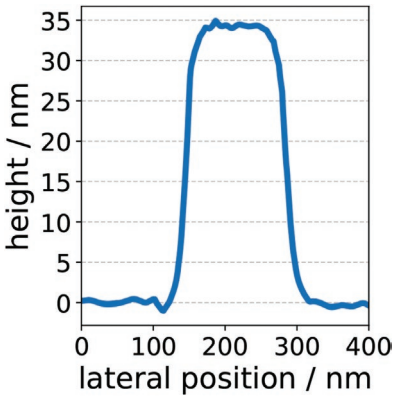

Figure 5. Representative AFM line scan of the separate cuboid.

stage with embedded capacitive sensors as a scanner and uses the classic optical lever technique to detect the bending and torsion of cantilevers. The AFM measurements are mostly performed in the intermittent-contact mode, where the amplitude modulation technique is applied for detecting the tip sample interaction. For achieving better CD measurement performance, a special probing strategy—referred to as vector approach probing (VAP)—has been developed and applied in the CD-AFM. Using this VAP method, the structure is probed in a pointwise manner by an AFM tip approaching along a 3D vector path, which is typically defined as the normal vector of the surface. During the probing process, the tip sample interaction curve is recorded for calculating the measurement result at each point. The VAP probing method offers advantages of (i) high 3D probing sensitivity and (ii) low tip wear, which are key and important for accurate 3D nanometrology. A previous study[36] had shown that the tip wear is less than 1 nm over more than 500 repeated measurements of a feature; the reproducibility of repeated feature characterizations is better than 1 nm. In addition, the CD-AFM applies an air bearing stage (referred to as *Nanostation 300*) for the coarse positioning of samples with a travel range of 550 mm × 300 mm. Thus, large samples such as silicon wafers and photomasks can be directly measured in the instrument. The air bearing is deactivated during AFM measurements to reduce its vibrational noise.

To ensure highly accurate and traceable measurements using the CD-AFM mentioned above, two important calibration issues have been performed in the study. The first issue concerns the traceable calibration of the scanner displacement, which is achieved by using sets of nanoscale standards, that is, the step height and grating standards. Prior to their usage, these standards were traceably calibrated by a metrological large-range AFM,[46] which serves as one of the main workhorses for primary dimensional nanometrology at the PTB. The second issue concerns the calibration of the tip geometry. The AFM tip geometry is a fundamental concern in CD-AFM measurements, as the image obtained in AFM measurements is the dilated result of a sample by the effective geometry of its tip. To derive the real geometry of the sample, the tip geometry must be reconstructed and then be corrected for from the measured AFM image. In this study, the calibration of the tip geometry is performed using the standard type *IVPS100-PTB*, whose geometry and corner rounding have been accurately and traceably calibrated to the lattice of crystal silicon by using high-resolution transmission electron microscopy,[47] jointly developed by the PTB and the company *Team-Nanotec*. The tip characterization methods and data processing procedures of the CD-AFM tip geometry were detailed in previous publication.[37] The method offers excellent measurement performance, for example, the tip geometry of a probe type *CDR120* with a nominal tip diameter of 120 nm is reconstructed using two different tip characterizers before, during, and after it is applied for a calibration of a user sample. The agreement of all 20 obtained tip profiles reaches 0.4 nm.[37] Thus, the dedicated instrumentation of the CD-AFM and calibration processes offers accurate and traceable calibration results of nanostructures, as illustrated in Table 2.

SEM Measurements: Sister samples (equivalent samples from the same EBL run) of the different nanostructures have been characterized using SEM with respect to their dimensional properties. The SEM measurements were carried out using a Zeiss LEO 1560 at Helmholtz-Zentrum Berlin.

Nano-XRF Set-Up: The experimental nano-XRF set-up includes a zone plate, beamstop, order sorting aperture (OSA) and samples, all on one single and compact platform,[48] avoiding unwanted relative motions of the components, and thus reducing the sensitivity of the set-up to vibrations. It is described schematically in Figure 1 and can be directly mounted onto the sample stage of an existing ultra-high vacuum-compatible instrumentation for reference-free XRF.[49] Through its size, this compact nano-XRF set-up offers various areas of operation as it allows for position-sensitive nano-XRF as well as scanning transmission X-ray microscopy (STXM) experiments. In addition, it can, of course, also be inserted in other experimental set-ups through their load-locks, if available.

The optical elements of the set-up consist of a Fresnel zone plate (with a diameter of 360 µm and 225 nm Au coating, an outer zone width of 25 nm and an integrated 50 µm central beam stop) and a 50 µm diameter OSA. The optics and the sample are mounted on piezo positioning stages, providing a nominal resolution of about 1 nm. The zone plate can be aligned in the X-Y plane, that is, perpendicular to the optical axis, and the OSA in X-Y-Z. Samples for XRF measurements are mounted on a 4-axis manipulator, which can be moved in and out of the beam path. Behind the sample position, a calibrated photodiode[50] allows for the determination of the incident photon flux and, optionally, STXM experiments.

For the experiments presented in this work, the compact nano-XRF set-up was placed 2m behind the focal position of the PTB's plane grating monochromator beamline[32] for undulator radiation at the electron storage ring BESSY II. The monochromatic photon energy of the incident X-ray radiation was E_0 = 1240 eV, that is, above the Ge-L_3 edge and just below the Ge-L_2 edge, thus avoiding the analytical challenges of Coster-Kronig transitions. Furthermore, pinholes can be placed in the beam path at the focus position of the beamline to confine and optimize the X-ray beam before the zone plate focuses it onto the sample plane. Depending on the required beam properties in regard to spatial resolution and intensity, the pinholes have different diameters. All presented results were achieved using a 50 µm pinhole. The emitted X-ray fluorescence radiation was detected by means of a calibrated[51,52] silicon drift detector (SDD) mounted at an angle of 90° with respect to the incident X-ray radiation. The nanostructure was scanned with a measurement time of 20 s for each lateral position, as well as a step size of 100 nm in both lateral directions, using the pre-characterized beam.

Beam Profile Determination: For the reference-free nano-XRF characterization of the germanium structures, it is crucial to determine the lateral intensity distribution of the nanofocused beam profile. The subsequent quantitative results depend directly on this information since different beam profile distributions and sizes may result in different footprints on the sample and, thus, different XRF signals. For that purpose, vertical and horizontal lines of different widths were used as dedicated test structures present on the same sample carrier for the characterization of the beam profile (**Figure 6**, *left*). On each of the widest lines (width about 500 nm), ten XRF line scans with a step size of 50 nm and a measurement time of 18 s per position were performed with a monochromatic photon energy of the incident X-ray radiation of E_0 = 1240 eV. The X-ray fluorescence photon flux for Ge-$L\alpha$ fluorescence radiation was derived from each recorded spectrum. As the EBL fabricated nanostructures have rather sharp edges, the slope of the X-ray fluorescence signal, when approaching a line, is a measure for the beam profile in that direction. This is supported by additional SEM images of the structures, which revealed only negligible deviations from a perfect knife-edge (below 20 nm). Furthermore, no significant deviations from the expected Gaussian beam profile were observed. Therefore, each line scan is modelled using the Gaussian error function (i.e., the normal cumulative distribution function) in order to derive the beam profile widths, cf. Figure 6 (*right*). The MC reconstruction approach described below is flexible enough to also handle non-Gaussian profiles. The

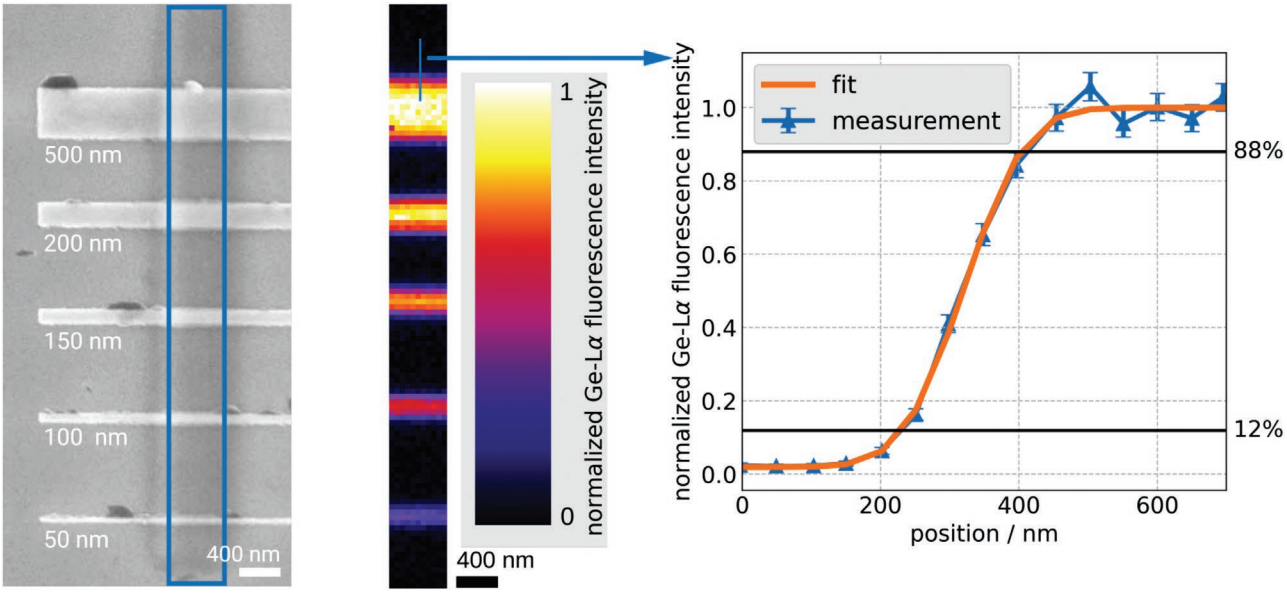

Figure 6. *Left*: SEM image of elongated rectangular germanium structures used for beam profile determination. Nominal vertical lengths are indicated under each structure. *Center*: Normalized Ge-Lα X-ray fluorescence micrograph of the indicated blue area of an identical germanium structure. *Right*: Normalized Ge-Lα X-ray fluorescence intensity of a selected line scan as indicated in the *center* image. Horizontal lines highlight the levels defining the FWHM.

modelling parameters for the presented beam profile determination are the distribution's amplitude, position, and width, as well as a constant background originating from stray light contributions. Exemplary results of the mean FWHM values determined from multiple line scans for the horizontal and vertical dimensions are:

hor. FWHM / nm	vert. FWHM / nm
162(6)	164(6)

The stated uncertainties are estimated from the standard deviation of the line scans of the respective edge. These used beam widths are constrained by the trade-off between the aim of high spatial resolution as well as high photon flux. With the current set-up, an FWHM of about 100 nm can be routinely achieved at a monochromatic photon flux of more than 10^{-8} s^{-1} (available on the sample). Smaller beams can be produced at the cost of disproportionately lower photon flux and, thus, longer measurement times. The primary limiting factor in regard to spatial resolution remains the impact of the beamline on the X-ray beam characteristics. A beamline optimized for radiometric applications in a wide spectral range[32] and not necessarily for transverse coherence-sensitive applications. To enhance coherence characteristics, sophisticated investigations are required, for example, by analyzing (and minimizing) vibrations of the monochromator[53] and optimizing beamline optics.

XRF Quantification Scheme: The reference-free XRF approach[27] allows for a direct quantification of the elemental mass thickness $\frac{m}{F}$ (g cm^{-2}), that is, elemental mass m per unit area F, using the measured X-ray fluorescence signals, as all relevant experimental, instrumental and atomic fundamental parameters are taken into account. The quantification can be performed using the Sherman equation[54,55] for a single homogeneous layer if the sample can be assumed to be infinitely extended, that is, laterally homogeneous at the length scale of the incident beam:

$$\frac{m}{F} = -\frac{1}{\mu_{\text{tot}}} \ln\left(1 - \frac{\Phi_{L\alpha}}{\Phi_0 Q \frac{\Omega_{\text{det}}}{4\pi} \frac{1}{\sin\psi_i} \frac{1}{\mu_{\text{tot}}}}\right) \quad (1)$$

with $Q = (\tau_{L_3,E_0} \cdot \omega_{L_3} \cdot g_{L\alpha})$ and $\mu_{\text{tot}} = \left(\frac{\mu_{E_0}}{\sin\psi_i} + \frac{\mu_{E_{L\alpha}}}{\sin\psi_o}\right)$. Here, μ_{E_0} is the mass attenuation coefficient at the excitation photon energy E_0, τ_{L_3,E_0} is the partial photoelectric cross-section of the L_3 absorption edge, ω_{L_3} is the fluorescence yield of the L_3 absorption edge, $\mu_{E_{L\alpha}}$ is the mass attenuation coefficient at the photon energy $E_{L\alpha}$ of the Lα fluorescence line, and $g_{L\alpha}$ is the transition probability of the Lα fluorescence line. Φ_0 is the photon flux of the incident radiation, $\Phi_{L\alpha} = \frac{R_{L\alpha}}{\varepsilon_{L\alpha}}$ is the photon flux of the Lα fluorescence line emitted into the solid angle of detection Ω_{det}, with the detected count rate $R_{L\alpha}$ and detection efficiency $\varepsilon_{L\alpha}$ at the photon energy $E_{L\alpha}$, ψ_i is the incident angle and ψ_o the observation angle.

The case of XRF based on a nanoscaled excitation beam illuminating a sample structure having similar dimensions is, however, more complex than for a laterally homogeneous sample. In general, the 3D shape of a nanoobject can be rather complex. Due to the nature of the measurement, a 2D map is recorded, where each measurement point corresponds to a different footprint, that is, a different partial overlap between the incident beam profile and the object. As a consequence, the convolution of the incident intensity distribution within the irradiated area and the 3D local mass thickness distribution needs to be taken into account for the XRF quantification. Furthermore, photon absorption paths inside the 3D sample depend on the lateral position of the incident beam with respect to the nanostructure: **Figure 7** depicts two photons, defined by their wave vectors $\mathbf{k}$ and $\mathbf{k}'$, both impinging on a cuboid sample under an incident angle ψ_i, but at different lateral positions. If, for example, both are absorbed in the same depth inside the sample, the path lengths (S and S') on their way to the point of absorption are substantially different. Equivalently, the maximum available absorption path for the incident photons ($S + A$ and $S' + A'$) depends strongly on both the incident beam position and the shape and size of the nanostructure. The same is true for the paths of X-ray fluorescence photons emitted in the direction of the detector. The probability for absorption of the emitted X-ray fluorescence photon scales with the available absorption path (S_B and S_B'). While only one lateral dimension is depicted in Figure 7, the aforementioned effects need to be considered for all spatial dimensions. These effects can substantially affect the observed X-ray fluorescence intensity, and Equation (1) is no longer applicable in that case.

To be able to account for these effects for an arbitrary shape of the nanostructure, a Monte Carlo (MC) method is employed. The geometrical path for a number of N photons is simulated (i.e., *ray tracing*). The simulation determines the fraction of N, which creates

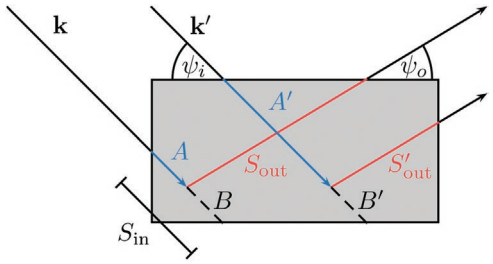

Figure 7. Schematic view of different photon paths inside a cuboid sample. For incident photons impinging under the same incident angle ψ_i, different absorption paths $S_{in} = (A + B) < (A' + B')$ are available, depending on the point of interaction. The outgoing X-ray fluorescence radiation is also differently attenuated, depending on the absorption paths $S_{out} > S'_{out}$.

X-ray fluorescence photons reaching the detector. The choice of N affects the simulation's computational cost and determines its desired numerical stability and accuracy. The approach is based on the MC method described by Schoonjans et al.[56] As extension to their software, our simulation allows for the definition of the nanostructure as a geometric shape, for example, a cuboid, with a given spatial position and dimensional parameters. These parameters will be varied during the fitting process as described below, and in that sense, they can be determined based on the measurement data. This approach allows accounting for nanostructures with essentially arbitrary shapes but may not be unambiguous for shapes which produce similar or identical X-ray fluorescence signals. In that case, additional experimental effort may be required to resolve these ambiguities, for example, by using multiple monochromatic incident photon energies in succession or by varying the angle of incidence or detection with respect to the specimen. Alternatively, independent insights can be gained by complementary measurements such as scanning probe and electron microscopy or from pre-existing knowledge of the manufacturing process.

Furthermore, the MC simulation defines incident photons by their monochromatic energy E_0 (here $E_0 = 1240$ eV) and a direction vector $\mathbf{k}$. The lateral coordinates of this direction vector are drawn randomly from a (normalized) 2D normal distribution, with the dimensions determined from the beam profile measurements. The probability that a photon interacts with the sample and that the X-ray fluorescence photon is not absorbed on the way out can be calculated according to the Beer-Lambert law using the path lengths from Figure 7. Depending on the position of the beam relative to the nanostructure, the effective available path S_{in} can also be zero if the incident photon is not incident on the nanostructure at all. This is true for a considerable number of photons during the measurements. Because of this, variance reduction techniques are applied similarly to those described by Schoonjans et al.[56] The actual penetration length A of an individual photon is calculated by

$$A = -\frac{\ln(1 - U p_A)}{\mu_{E_0} \rho} \tag{2}$$

where $0 \leqslant U < 1$ is a random number drawn from a uniform distribution. In practice, though, U is calculated by a pseudorandom number generator. The probability p_A that the incident photon is absorbed in the sample (i.e., interacts with the sample), is calculated using the Beer-Lambert law:

$$p_A = 1 - \exp\left(-\mu_{E_0} \rho S_{in}\right) \tag{3}$$

The total available absorption path S_{in} for the incident photon is determined by its direction vector $\mathbf{k}$ and the position, shape and size of the sample. The total number of photons of the $L\alpha$ fluorescence line per second emitted into the solid angle of the detector is then given by

$$\Phi_{L\alpha} = \Phi_0 \frac{Q}{\mu_{E_0}} \frac{\Omega_{det}}{4\pi} \bar{p}. \tag{4}$$

Here, the fraction $\frac{Q}{\mu_{E_0}}$ describes the probability that an interacting photon produces radiation of the correct X-ray fluorescence line. The probability $\bar{p}$ is given by the number of photons interacting with the sample and *not* getting absorbed in the sample, averaged over all simulated N photons, as given by the following Equation (5):

$$\bar{p} = \frac{1}{N} \sum_N p_A \exp\left(-\mu_{E_{L\alpha}} \rho S_{out}\right) \tag{5}$$

Equation (4) is a generalization of the original Sherman Equation (1) and is used for the fitting process described in the following. In general, the local mass thickness distribution can be arbitrarily complex for a given nanostructure. The present nanostructures were purposefully designed to be rather simple structures so that the used production process can create them with reproducible accuracy and the performance of the approach itself could be easily evaluated. Since additional validation measurements confirmed sharp edges (cf. SEM images in Figure 2 and AFM measurement in Figure 5), a homogeneous regular cuboid can be assumed as a model for the nanoobject. Thus, the present nanostructure can be described using decidedly few model parameters: Two location parameters (X- and Y-position) and 3D size parameters (width, length, and height of the cuboid). More complex sample systems certainly increase the number of model parameters required and, in turn, the computational effort. However, this approach can also be used for inhomogeneous objects with locally varying mass thicknesses. Since the positional parameters are arbitrary and depend on the position during the experiment, the parameters of interest are the dimensional sizes. The height h is related to the mass thickness by $\frac{m}{F} = (h \cdot \rho)$. Here, the germanium density $\rho = 4.65(24)$ g cm^{-3} was independently determined by modelling of XRR data. This XRR data was obtained by using a non-nanofocused beam geometry on a large germanium layer (50 µm width and several mm length) at the edge of the structured area, which can be used as a proxy for the nanostructured sample due to the homogeneity of the production process.

Acknowledgements

Part of this work was supported by the EMPIR programme, co-financed by the Participating States and from the Horizon 2020 research and innovation programme from the European Union, through grant agreement 20FUN06 MEMQuD. This project has received funding from the Electronic Component Systems for European Leadership Joint Undertaking under grant agreement No 826589–MADEin4. This joint undertaking receives support from the European Union's Horizon 2020 research and innovation programme and the Netherlands, France, Belgium, Germany, Czech Republic, Austria, Hungary, and Israel. We gratefully acknowledge the support from the Deutsche Forschungsgemeinschaft (DFG, German Research Foundation)–Project-ID 372486779–SFB 1340.

Open access funding enabled and organized by Projekt DEAL.

Conflict of Interest

The authors declare no conflict of interest.

Data Availability Statement

The data that support the findings of this study are available from the corresponding author upon reasonable request.

Keywords

nanobeam X-ray fluorescence (XRF), nanometrology, nanostructure characterization, quantitative analysis

Received: August 11, 2022
Revised: November 22, 2022
Published online: December 15, 2022

[1] A. Barhoum, M. L. García-Betancourt, J. Jeevanandam, E. A. Hussien, S. A. Mekkawy, M. Mostafa, M. M. Omran, M. S. Abdalla, M. Bechelany, *Nanomaterials* **2022**, *12*, 2.
[2] S. Talebian, T. Rodrigues, J. das Neves, B. Sarmento, R. Langer, J. Conde, *ACS Nano* **2021**, *15*, 15940.
[3] E. Pomerantseva, F. Bonaccorso, X. Feng, Y. Cui, Y. Gogotsi, *Science* **2019**, *366*, eaan8285.
[4] S. Kim, G. Myeong, W. Shin, H. Lim, B. Kim, T. Jin, S. Chang, K. Watanabe, T. Taniguchi, S. Cho, *Nat. Nanotechnol.* **2020**, *15*, 203.
[5] A. Veloso, G. Eneman, T. Huynh-Bao, A. Chasin, E. Simoen, E. Vecchio, K. Devriendt, S. Brus, E. Rosseel, A. Hikavyy, et al. in *2019 IEEE International Electron Devices Meeting (IEDM)*, IEEE, Piscataway **2019**, pp. 11–1.
[6] S. Natarajan, M. Agostinelli, S. Akbar, M. Bost, A. Bowonder, V. Chikarmane, S. Chouksey, A. Dasgupta, K. Fischer, Q. Fu, et al., in *2014 IEEE International Electron Devices Meeting*, IEEE, Piscataway **2014**, pp. 3–7.
[7] N. Loubet, T. Hook, P. Montanini, C.-W. Yeung, S. Kanakasabapathy, M. Guillom, T. Yamashita, J. Zhang, X. Miao, J. Wang, A. Young, R. Chao, M. Kang, Z. Liu, S. Fan, B. Hamieh, S. Sieg, Y. Mignot, W. Xu, S.-C. Seo, J. Yoo, S. Mochizuki, M. Sankarapandian, O. Kwon, A. Carr, A. Greene, Y. Park, J. Frougier, R. Galatage, R. Bao, et al.in *2017 Symposium on VLSI Technology*, IEEE, Piscataway **2017**, pp. T230–T231.
[8] J. Ryckaert, P. Schuddinck, P. Weckx, G. Bouche, B. Vincent, J. Smith, Y. Sherazi, A. Mallik, H. Mertens, S. Demuynck, et al., in *2018 IEEE Symposium on VLSI Technology*, IEEE, Piscataway **2018**, pp. 141–142.
[9] H. Liu, Y. Dong, M. J. Cherukara, K. Sasikumar, B. Narayanan, Z. Cai, B. Lai, L. Stan, S. Hong, M. K. Y. Chan, S. K. Sankaranarayanan, H. Zhou, D. D. Fong, *ACS Nano* **2018**, *12*, 4938.
[10] N. G. Orji, M. Badaroglu, B. M. Barnes, C. Beitia, B. D. Bunday, U. Celano, R. J. Kline, M. Neisser, Y. Obeng, A. E. Vladar, *Nat. Electron.* **2018**, *1*, 532.
[11] P. Linkov, M. Artemyev, A. E. Efimov, I. Nabiev, *Nanoscale* **2013**, *5*, 8781.
[12] J. A. Liddle, G. M. Gallatin, *ACS Nano* **2016**, *10*, 2995.
[13] G. L. Hornyak, J. J. Moore, H. F. Tibbals, J. Dutta, in *Fundamentals of Nanotechnology*, CRC Press, Boca Raton, FL **2018**.
[14] B. Bunday, G. Orji, in *2021 IEEE International Roadmap for Devices and Systems Outbriefs*, IEEE, Piscataway **2021**, pp. 01–68.
[15] M. A. Breton, D. Schmidt, A. Greene, J. Frougier, N. Felix, *J. Micro/Nanopatt. Mater. Metrol.* **2022**, *21*, 021206.
[16] C. Sanchez-Cano, R. A. Alvarez-Puebla, J. M. Abendroth, T. Beck, R. Blick, Y. Cao, F. Caruso, I. Chakraborty, H. N. Chapman, C. Chen, B. E. Cohen, A. L. C. Conceição, D. P. Cormode, D. Cui, K. A. Dawson, G. Falkenberg, C. Fan, N. Feliu, M. Gao, E. Gargioni, C.-C. Glüer, F. Grüner, M. Hassan, Y. Hu, Y. Huang, S. Huber, N. Huse, Y. Kang, A. Khademhosseini, T. F. Keller, et al., *ACS Nano* **2021**, *15*, 3754.
[17] C. Cao, M. F. Toney, T.-K. Sham, R. Harder, P. R. Shearing, X. Xiao, J. Wang, *Mater. Today* **2020**, *34*, 132.
[18] B. M. West, M. Stuckelberger, A. Jeffries, S. Gangam, B. Lai, B. Stripe, J. Maser, V. Rose, S. Vogt, M. I. Bertoni, *J. Synchrotron Radiation* **2017**, *24*, 288.
[19] P. Hönicke, Y. Kayser, K. V. Nikolaev, V. Soltwisch, J. E. Scheerder, C. Fleischmann, T. Siefke, A. Andrle, G. Gwalt, F. Siewert, J. Davis, M. Huth, A. Veloso, R. Loo, D. Skroblin, M. Steinert, A. Undisz, M. Rettenmayr, B. Beckhoff, *Small* **2022**, *18*, 2105776.
[20] A. Andrle, P. Hönicke, G. Gwalt, P.-I. Schneider, Y. Kayser, F. Siewert, V. Soltwisch, *Nanomaterials* **2021**, *11*, 1647.
[21] L. Lemelle, A. Simionovici, T. Schoonjans, R. Tucoulou, E. Enrico, M. Salomé, A. Hofmann, B. Cavalazzi, *Trends Analyt. Chem.* **2017**, *91*, 104.
[22] B. D. Samber, E. Meul, B. Laforce, B. D. Paepe, J. Smet, M. D. Bruyne, R. D. Rycke, S. Bohic, P. Cloetens, R. V. Coster, P. Vandenabeele, T. V. Berghe, *PLOS ONE* **2018**, *13*, e0190495.
[23] C. Gramaccioni, Y. Yang, A. Procopio, A. Pacureanu, S. Bohic, E. Malucelli, S. Iotti, G. Farruggia, I. Bukreeva, A. Notargiacomo, M. Fratini, P. Valenti, L. Rosa, F. Berlutti, P. Cloetens, S. Lagomarsino, *Appl. Phys. Lett.* **2018**, *112*, 053701.
[24] G. Roebben, K. Rasmussen, V. Kestens, T. P. J. Linsinger, H. Rauscher, H. Emons, H. Stamm, *J. Nanopart. Res.* **2013**, *15*, 1455.
[25] L. J. Johnston, N. Gonzalez-Rojano, K. J. Wilkinson, B. Xing, *NanoImpact* **2020**, *18*, 100219.
[26] S. López-Sanz, F. J. Guzmán Bernardo, R. C. Rodríguez Martín-Doimeadios, Á. Ríos, *Anal. Chim. Acta* **2019**, *1059*, 1.
[27] B. Beckhoff, *J. Anal. At. Spectrom.* **2008**, *23*, 845.
[28] P. Hönicke, M. Krämer, L. Lühl, K. Andrianov, B. Beckhoff, R. Dietsch, T. Holz, B. Kanngiesser, D. Weißbach, T. Wilhein, *Spectrochim. Acta B: At. Spectrosc.* **2018**, *145*, 36.
[29] B. Beckhoff, *Nanomaterials* **2022**, *12*, 2255.
[30] T. W. Victor, L. M. Easthon, M. Ge, K. H. O'Toole, R. J. Smith, X. Huang, H. Yan, K. N. Allen, Y. S. Chu, L. M. Miller, *Sci. Rep.* **2018**, *8*, 13415.
[31] J. Schoon, B. Hesse, A. Rakow, M. J. Ort, A. Lagrange, D. Jacobi, A. Winter, K. Huesker, S. Reinke, M. Cotte, R. Tucoulou, U. Marx, C. Perka, G. N. Duda, S. Geissler, *Adv. Sci.* **2020**, *7*, 2000412.
[32] F. Senf, U. Flechsig, F. Eggenstein, W. Gudat, R. Klein, H. Rabus, G. Ulm, *J. Synchrotron Rad.* **1998**, *5*, 780.
[33] J. Baumann, Y. Kayser, B. Kanngießer, *Phys. Status Solidi B* **2021**, *258*, 2000471.
[34] R. Unterumsberger, B. Beckhoff, A. Gross, H. Stosnach, S. Nowak, Y. P. Stenzel, M. Krämer, A. von Bohlen, *J. Anal. At. Spectrom.* **2021**, *36*, 1933.
[35] D. Foreman-Mackey, D. W. Hogg, D. Lang, J. Goodman, *Publ. Astron. Soc. Pac.* **2013**, *125*, 306.
[36] G. Dai, W. Hässler-Grohne, D. Hueser, H. Wolff, J. Flügge, H. Bosse, *J. Micro/Nanolithogr. MEMS MOEMS* **2012**, *11*, 1.
[37] G. Dai, L. Xu, K. Hahm, *Meas. Sci. Technol.* **2020**, *31*, 074011.
[38] N. Shah, in *Proceedings of the Future Technologies Conference (FTC) 2020*, (Eds: K. Arai, S. Kapoor, R. Bhatia), Vol. *2*, Springer, Cham **2021**, pp. 340–346.
[39] S. Barraud, B. Previtali, C. Vizioz, J. M. Hartmann, J. Sturm, J. Lassarre, C. Perrot, P. Rodriguez, V. Loup, A. Magalhaes-Lucas, R. Kies, G. Romano, M. Cassé, N. Bernier, A. Jannaud, A. Grenier, F. Andrieu, in *2020 IEEE Symposium on VLSI Technology*, IEEE, Piscataway **2020**, pp. 1–2.
[40] G. Hills, M. G. Bardon, G. Doornbos, D. Yakimets, P. Schuddinck, R. Baert, D. Jang, L. Mattii, S. M. Y. Sherazi, D. Rodopoulos, R. Ritzenthaler, C.-S. Lee, A. V.-Y. Thean, I. Radu, A. Spessot, P. Debacker, F. Catthoor, P. Raghavan, M. M. Shulaker, H.-S. P. Wong, S. Mitra, *IEEE Trans. Nanotechnol.* **2018**, *17*, 1259.
[41] P. Weckx, J. Ryckaert, E. D. Litta, D. Yakimets, P. Matagne, P. Schuddinck, D. Jang, B. Chehab, R. Baert, M. Gupta, Y. Oniki, L.-A. Ragnarsson, N. Horiguchi, A. Spessot, D. Verkest, in *2019 IEEE International Electron Devices Meeting (IEDM)*, IEEE, Piscataway **2019**, pp. 36.5.1–36.5.4.
[42] B. Rösner, S. Finizio, F. Koch, F. Döring, V. A. Guzenko, M. Langer, E. Kirk, B. Watts, M. Meyer, J. L. na Ornelas, A. Späth, S. Stanescu,

S. Swaraj, R. Belkhou, T. Ishikawa, T. F. Keller, B. Gross, M. Poggio, R. H. Fink, J. Raabe, A. Kleibert, C. David, *Optica* **2020**, *7*, 1602.
[43] D. E. Newbury, N. W. M. Ritchie, *Scanning* **2013**, *35*, 141.
[44] V. Rackwitz, M. Ostermann, U. Panne, V.-D. Hodoroaba, *J. Anal. At. Spectrom.* **2013**, *28*, 1466.
[45] L. Lühl, K. Andrianov, H. Dierks, A. Haidl, A. Dehlinger, M. Heine, J. Heeren, T. Nisius, T. Wilhein, B. Kanngießer, *J. Synchrotron Rad.* **2019**, *26*, 430.
[46] G. Dai, H. Wolff, F. Pohlenz, H.-U. Danzebrink, *Rev. Sci. Instrum.* **2009**, *80*, 043702.
[47] G. Dai, F. Zhu, M. Heidelmann, G. Fritz, T. Bayer, S. Kalt, J. Fluegge, *Meas. Sci. Technol.* **2015**, *26*, 115006.
[48] J. Lubeck, C. Seim, A. Dehlinger, A. Haidl, P. Hönicke, Y. Kayser, R. Unterumsberger, C. Fleischmann, B. Beckhoff, *Microsc. Microanal.* **2018**, *24*, 162.
[49] J. Lubeck, B. Beckhoff, R. Fliegauf, I. Holfelder, P. Hönicke, M. Müller, B. Pollakowski, F. Reinhardt, J. Eser, *Rev. Sci. Instrum.* **2013**, *84*, 045106.
[50] A. Gottwald, U. Kroth, M. Krumrey, M. Richter, F. Scholze, G. Ulm, *Metrologia* **2006**, *43*, S125.
[51] F. Scholze, M. Procop, *X-Ray Spectrom.* **2001**, *30*, 69.
[52] F. Scholze, M. Procop, *X-Ray Spectrom.* **2009**, *38*, 312.
[53] K. Bagschik, J. Wagner, R. Buß, M. Riepp, A. Philippi-Kobs, L. Müller, J. Buck, F. Trinter, F. Scholz, J. Seltmann, M. Hoesch, J. Viefhaus, G. Grübel, H. P. Oepen, R. Frömter, *Opt. Exp.* **2020**, *28*, 7282.
[54] J. Sherman, *Spectrochim. Acta* **1955**, *7*, 283.
[55] D. K. G. de Boer, *X-Ray Spectrom.* **1990**, *19*, 145.
[56] T. Schoonjans, L. Vincze, V. A. Solé, M. Sanchez del Rio, P. Brondeel, G. Silversmit, K. Appel, C. Ferrero, *Spectrochim. Acta B: At. Spectrosc.* **2012**, *70*, 10.